

Article

The Design and Preclinical Evaluation of a Single-Label Bimodal Nanobody Tracer for Image-Guided Surgery

Pieterjan Debie ¹, Noemi B. Declerck ¹, Danny van Willigen ², Celine M. Huygen ¹, Bieke De Sloovere ¹, Lukasz Mateusiak ¹, Jessica Bridoux ¹, Janik Puttemans ¹, Nick Devoogdt ¹, Fijs W. B. van Leeuwen ² and Sophie Hernot ^{1,*}

- ¹ Laboratory for In Vivo Cellular and Molecular Imaging, ICMI-BEFY, Vrije Universiteit Brussel, Laarbeeklaan 103, 1090 Brussels, Belgium; pieterjan.debie91@gmail.com (P.D.); Noemi.Berte.Declerck@vub.be (N.B.D.); Celine.Marina.Huygen@vub.be (C.M.H.); bieke.de.sloovere@hotmail.com (B.D.S.); Lukasz.Mateusiak@vub.be (L.M.); Jessica.Bridoux@vub.be (J.B.); Janik.Puttemans@vub.be (J.P.); ndevogdt@vub.be (N.D.)
- ² Leiden University Medical Center, Interventional Molecular Imaging Laboratory, Department of Radiology, Leiden University, 2311 Leiden, The Netherlands; d.m.van_willigen@lumc.nl (D.v.W.); f.w.b.van_leeuwen@lumc.nl (F.W.B.v.L.)
- * Correspondence: Sophie.Hernot@vub.be; Tel.: +32-2477-4991



Citation: Debie, P.; Declerck, N.B.; van Willigen, D.; Huygen, C.M.; De Sloovere, B.; Mateusiak, L.; Bridoux, J.; Puttemans, J.; Devoogdt, N.; van Leeuwen, F.W.B.; et al. The Design and Preclinical Evaluation of a Single-Label Bimodal Nanobody Tracer for Image-Guided Surgery. *Biomolecules* **2021**, *11*, 360. <https://doi.org/10.3390/biom11030360>

Academic Editor: Vladimir N. Uversky

Received: 26 January 2021
Accepted: 23 February 2021
Published: 26 February 2021

Publisher's Note: MDPI stays neutral with regard to jurisdictional claims in published maps and institutional affiliations.



Copyright: © 2021 by the authors. Licensee MDPI, Basel, Switzerland. This article is an open access article distributed under the terms and conditions of the Creative Commons Attribution (CC BY) license (<https://creativecommons.org/licenses/by/4.0/>).

Abstract: Intraoperative guidance using targeted fluorescent tracers can potentially provide surgeons with real-time feedback on the presence of tumor tissue in resection margins. To overcome the limited depth penetration of fluorescent light, combining fluorescence with SPECT/CT imaging and/or gamma-ray tracing has been proposed. Here, we describe the design and preclinical validation of a novel bimodal nanobody-tracer, labeled using a “multifunctional single attachment point” (MSAP) label, integrating a Cy5 fluorophore and a diethylenetriaminopentaacetic acid (DTPA) chelator into a single structure. After conjugation of the bimodal MSAP to primary amines of the anti-HER2 nanobody 2Rs15d and ¹¹¹In-labeling of DTPA, the tracer’s characteristics were evaluated in vitro. Subsequently, its biodistribution and tumor targeting were assessed by SPECT/CT and fluorescence imaging over 24 h. Finally, the tracer’s ability to identify small, disseminated tumor lesions was investigated in mice bearing HER2-overexpressing SKOV3.IP1 peritoneal lesions. [¹¹¹In]In-MSAP.2Rs15d retained its affinity following conjugation and remained stable for 24 h. In vivo SPECT/CT and fluorescence images showed specific uptake in HER2-overexpressing tumors with low background. High tumor-to-muscle ratios were obtained at 1h p.i. and remained 19-fold on SPECT/CT and 3-fold on fluorescence images over 24 h. In the intraperitoneally disseminated model, the tracer allowed detection of larger lesions via nuclear imaging, while fluorescence enabled accurate removal of submillimeter lesions. Bimodal nuclear/fluorescent nanobody-tracers can thus be conveniently designed by conjugation of a single-molecule MSAP-reagent carrying a fluorophore and chelator for radioactive labeling. Such tracers hold promise for clinical applications.

Keywords: single-domain antibodies; fluorescence-guided surgery; molecular imaging; hybrid imaging

1. Introduction

Intraoperative guidance with targeted fluorescent contrast agents is an emerging tool to achieve more complete removal of malignant tissue in oncologic surgery due to its unique capability to provide real-time visual feedback to the surgeon about tumor margins and local invasion [1]. Nevertheless, the technique is limited to the detection of superficial lesions or lesions lying at most a centimeter deep in tissue, despite the deeper tissue penetration of fluorescent signals with excitation and emission in the far-red and near-infrared region as compared to a lower wavelength visible light [2]. Therefore, hybrid imaging combining fluorescence imaging with diagnostic nuclear medicine techniques has

shown to be of great value in preclinical and clinical studies, as the latter can provide depth-independent information through emission of gamma-radiation [3–7]. The radioactive component can either be used for preoperative imaging in order to better plan surgery or can provide additional guidance during the surgery itself via gamma probe detection (real-time auditive feedback).

To design a targeted tracer that can be detected with both modalities, i.e., a bimodal tracer, the most straightforward method would be by randomly conjugating a fluorophore and chelator/prosthetic group directly to the targeting moiety. This strategy has been used for antibodies or large antibody fragments [8–11]. It does, however, lead to heterogeneous functionalization rates of the different labels, making it complex to standardize the tracer's composition. For targeting moieties such as small antibody fragments, peptides and small molecules that only have a limited number of conjugation sites, the conjugation of multiple labels can have a more pronounced detrimental effect on their functionality and biodistribution, leading to the introduction of single bimodal labels [12]. The integration of both a fluorescent dye and a chelator for radioactive labeling into a single backbone structure has been pursued in a range of designs. One often bimodal label design is based on the so-called "multifunctional single attachment point" (MSAP) design introduced by Garanger et al., consisting of an amino acid backbone modified to bear a fluorophore, a chelator for radiolabeling, and a reactive group for conjugation [13]. Originally the MSAP label was used to create hybrid peptides such as cRGD targeting integrins and Ac-TZ14011 against CXCR4 labeled with Cy5.5/¹¹¹In for the imaging in breast cancer models [12,14,15]. Later the backbone [16] and the fluorescent dyes in this label were varied [17,18] and it was even applied to antibodies [19,20].

While antibodies and peptides are commonly used tracers in molecular imaging and fluorescence-guided surgery, these compounds may have certain drawbacks. Antibodies circulate in the blood after intravenous injection for several weeks, causing high background signal and late imaging timepoints (several days) [21]. Peptides often have faster kinetics and are easier to synthesize, however, their small size makes it so their biodistribution can be heavily influenced by the chemical composition of the diagnostic labels [17]. An alternative to these targeting moieties is the use of Nanobodies. Nanobodies are the smallest stable antigen fragments, derived from camelid heavy-chain only antibodies [22]. They can be conveniently generated against molecular targets through in vivo affinity maturation and possess interesting properties for imaging [23–26]. Mainly, through their fast blood clearance and rapid, homogenous target binding, nanobody-tracers achieve high target-to-background ratios from 1 h post-injection in both fluorescent and nuclear molecular imaging applications [27–32]. To overcome the limitations of single labeled agents for image-guided surgery as discussed above, in this paper, we describe a bimodal nuclear/fluorescent nanobody-tracer based on a custom MSAP label (Figure 1) and report its preclinical validation for the pre- and intraoperative imaging. The human epidermal growth factor receptor 2 (HER2) was chosen as target for this proof-of-concept study given the availability of the well-characterized anti-HER2 Nanobody 2Rs15d [32].

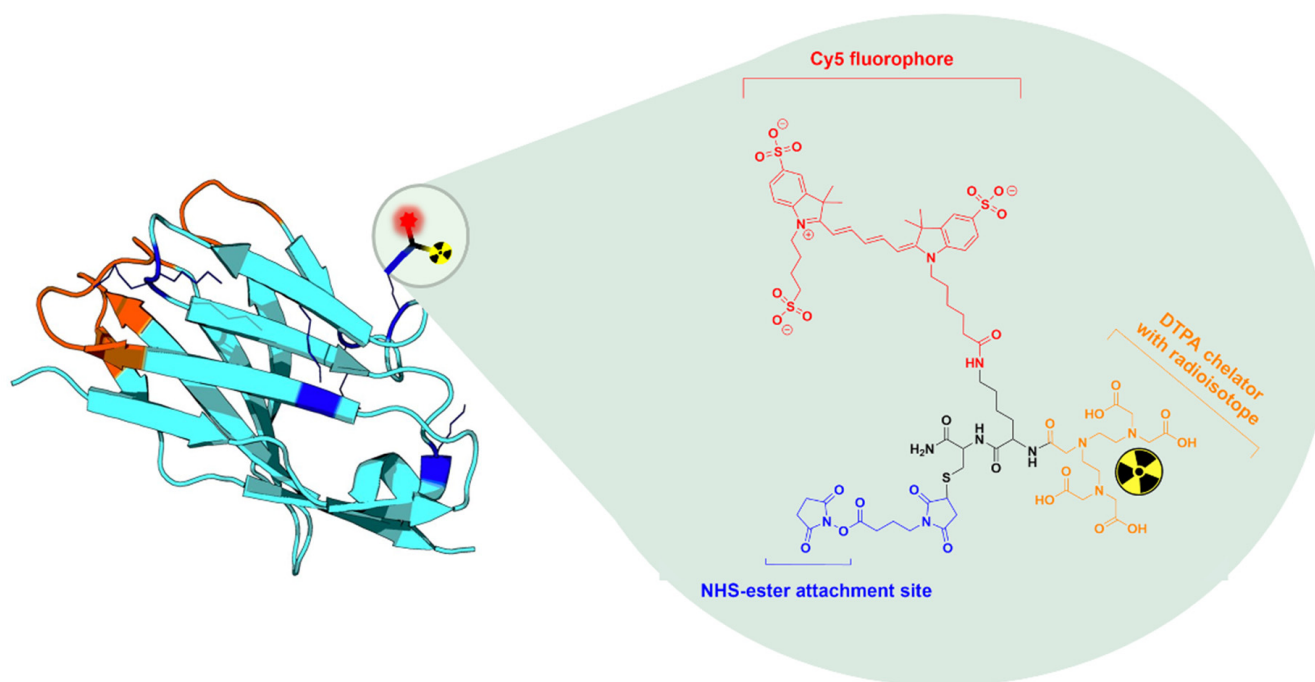


Figure 1. Schematic representation of the anti-HER2 Nanobody 2Rs15d being randomly labeled on its lysines via NHS-chemistry (blue) with the MSAP containing a Cy5 dye (red) and a DTPA-chelator complexed with an Indium-111 (^{111}In) radioisotope (yellow). The MSAP analogue's backbone is displayed in black.

2. Materials and Methods

2.1. Production and MSAP-Conjugation of Nanobodies

The used HER2-specific Nanobody 2Rs15d has been generated in a previous study [32] and was expressed and purified without a C-terminal hexahistidine-tag [33]. The NHS-ester functionalized MSAP molecule (Figure 1), which consists of a peptide scaffold bearing a trisulphonated Cy5 fluorophore (wavelength of maximal absorption/emission: 646/662 nm [34]) and a pentetic acid (diethylenetriaminepentaacetic acid, DTPA) chelator, was synthesized as previously described [17]. For MSAP conjugation to the primary amines on the Nanobody, 1 mg of 2Rs15d was incubated with a $1.2\times$ molar excess of MSAP in 1 mL of 0.1 M K_2HPO_4 (Merck KGaA, Darmstadt, Germany) buffer at a final pH of 8.3–8.5. The conjugated Nanobody MSAP.2Rs15d was then purified using size-exclusion chromatography (SEC) on a Superdex 75 10/300GL column (GE Healthcare, Chicago, IL, USA) with 0.1 M NH_4OAc (Acros Organics, Fair Lawn, NJ, USA) pH 7 as running buffer (0.5 mL/min). Quality control runs of the purified MSAP.2Rs15d were performed on a Superdex 75 5/150GL column with PBS pH 7.4 as running buffer (0.3 mL/min). All buffers were treated with 2 g/L chelex (Merck KGaA) before use.

One MSAP molecule contains exactly one DTPA chelator and one fluorophore, thus we can determine the MSAP degree of labeling (DOL) of the compound using the fluorophore's concentration. Therefore, the DOL was calculated as the ratio of the fluorophore's to the Nanobody's concentration. This was determined by absorbance measurement at 650 and 280 nm, respectively (Nanodrop 2000 spectrophotometer, Thermo Fisher Scientific). To account for the absorbance contribution of the fluorophore and the chelator at 280 nm, the measured absorbance at 280 nm was corrected by subtracting it with 5% of the absorbance value at 650 nm.

2.2. Radiolabeling of MSAP-Nanobody Construct

For ^{111}In -labeling, 5–120 μL of ^{111}In (Curium Pharma, Petten, The Netherlands) as an aqueous solution in 0.05 M HCl (6.8–26.3 MBq) was added to the MSAP.2Rs15d construct (5 μM final concentration) and 0.2 M NH_4OAc buffer pH 5.0, in a final volume

of 35–500 μL at pH 4.5. The reaction mixture was incubated for 30 min at 50 °C [35]. After radiolabeling, the product was filtered using a 0.2 μm filter (PALL Corporation, Port Washington, NY, USA). Radiochemical purity was determined by instant thin layer chromatography (iTLC) using 0.1 M sodium citrate as mobile phase. Chemical identity of [^{111}In]In-MSAP.2Rs15d (5 μg diluted in PBS with 0.1% Tween[®] 80 detergent) was confirmed by analytical SEC on a Superdex 75 5/150GL column using PBS pH 7.4 as running buffer. Radioactivity was detected online using a Gabi detector (Elysia-Raytest, Angleur, Belgium) and was compared to the absorbance measured at 280 (Nanobody) and 650 (Cy5) nm. Stability of the bimodal tracer was furthermore evaluated by SEC after 24 h incubation in PBS at room temperature or in human serum at 37 °C.

2.3. In Vitro Functionality

The binding kinetics of MSAP.2Rs15d were evaluated through surface plasmon resonance (SPR) using Biacore T200 (GE Healthcare), as previously described [32]. Briefly, recombinant HER2-Fc protein was immobilized on a CM5 chip, then sensorgrams were generated for a $\frac{1}{2}$ dilution series of MSAP.2Rs15d in HEPES buffered saline (HBS), ranging from 2.0×10^{-7} M to 1.6×10^{-9} M.

The specificity of the compound was further validated by a fluorescence-based cell-binding study, using HER2-overexpressing SKOV3 and HER2-negative control Chinese hamster ovarian (CHO) cells. SKOV3 and CHO cells were seeded in 24-well plates at 100,000 cells/well and incubated at 37 °C and 5% CO_2 for 48 h. MSAP.2Rs15d was added at a final concentration of 1.1×10^{-8} M to wells with SKOV3 cells, CHO cells, or coincubated on SKOV3 cells with a 100-fold molar excess of unmodified 2Rs15d Nanobody. The cells were then incubated for 2 h at 4 °C, washed and remaining fluorescence in the wells was measured in the 700 nm channel of a flatbed fluorescence scanner (Odyssey, LI-COR Biosciences, Lincoln, Nebraska). For each condition three replicates were included.

To determine the affinity (K_D) of [^{111}In]In-MSAP.2Rs15d after radiolabeling, a saturation cell-binding study was performed using HER2 overexpressing SKOV3 cells. Cells were seeded in 24-well plates at 100,000 cells/well and incubated at 37 °C with 5% CO_2 for 48 h. After ^{111}In -labeling, a 1/3 dilution series (ranging from 1.0×10^{-7} M to 4.6×10^{-11} M, in triplicate) of [^{111}In]In-MSAP.2Rs15d was added to the cells, either with or without a 100 \times molar excess of unlabeled 2Rs15d. After 1 h of incubation at 4 °C, the wells were washed, and cells were detached using 1 M NaOH. The bound activity was then measured using a gamma counter (Wizard2 2480, Perkin Elmer, Waltham, MA, USA).

2.4. In Vivo Biodistribution and Tumor Targeting Potential Using Bimodal Imaging

All animal experiments were approved by the Ethical Committee for Animal Experiments of the Vrije Universiteit Brussel (project nr. 15-272-5). The mice were housed in individually ventilated cages at 19–24 °C in 40–60% humidity with a light/dark cycle of 14/10 h. Low fluorescence food pellets (Teklad 2016, Envigo, Indianapolis, IN, USA) and water were provided ad libitum.

2.4.1. Longitudinal Biodistribution Study in Subcutaneous Xenografts

SKOV3 (10×10^6 cells) or HER2-negative MDA-MB-435S (2×10^6 cells) subcutaneous tumors were implanted on the right flank of female athymic nude Crl:NU-Foxn1^{nu} mice (Charles River, $n = 3$ per group), and grown until the tumors for all animals within a group reached a volume between 100 and 500 mm^3 .

Of [^{111}In]In-MSAP.2Rs15d 7.5 μg (12.3 ± 0.5 MBq, corresponding to 1 nmol MSAP, and apparent molar specific activity of 13.5 ± 0.6 GBq/ μmol) was injected via the tail vein of either SKOV3 or MDA-MB-435S xenograft bearing mice. Consecutive single photon emission computed tomography/computed tomography (SPECT/CT) scans were performed at 1, 4, and 24 h post-injection, and after each scan, the same animal was subjected to fluorescence imaging. After the final timepoint, animals were killed by cervical dislocation for further ex vivo biodistribution studies. Fluorescence imaging of individual organs

and tissues was performed, whereafter the organs and tissues were weighed, and their radioactive signal measured using a gamma counter (Wizard2 2480, Perkin Elmer). Results were decay-corrected and expressed as percentage of injected dose per cm^3 (%ID/ cm^3).

2.4.2. Image-Guided Resection of Intraperitoneally Disseminated Tumor Lesions

Luciferase-expressing SKOV3.IP1 cells (0.5×10^6), kindly provided by Prof. Marc Bracke (UGent, Belgium), were intraperitoneally injected in Crl: NU-Foxn1^{Nu} mice (Charles River; $n = 3$) [30,36]. Tumor growth was followed-up using bioluminescence imaging for 30 days. [¹¹¹In]In-MSAP.2Rs15d (10.5 ± 0.5 MBq, 7.5 μg corresponding to 1 nmol MSAP, and apparent molar specific activity of 11.6 ± 0.5 GBq/ μmol , intravenously) and luciferin (150 mg/kg, intraperitoneally) were administered 1 h and 10 min, respectively prior to SPECT/CT imaging. Then, the animals were killed via cervical dislocation and peritoneal tumor lesions were resected under fluorescence guidance. Finally, fluorescence and radioactive signals of all confirmed tumor lesions, and of the major peritoneal organs were measured *ex vivo* as described in 2.4.1 and 2.5. Bioluminescence imaging (BLI) (PhotonIMAGERTM Optima, Biospace, Nesles la Vallée, France) was used to confirm the tumorous character of resected lesions.

2.5. Imaging Protocols

During all imaging procedures, for intravenous injections and for cervical dislocation, mice were anaesthetized with isoflurane gas (5% for induction, 2% for maintenance during the scan, 0.5–1.0 mL/min oxygen flow rate). MicroSPECT/CT imaging was performed using a Vector⁺ system (Milabs) equipped with a general-purpose rat/mouse 1.5 mm 75 pinhole collimator. Scans were performed in spiral mode with 6 bed positions and an acquisition time of 200 s per bed position. For image reconstruction, 2 subsets and 4 iterations were used, with a voxel size of 0.4 mm in U-SPECT-Rec software (Milabs). The CT scan was made in 1 bed position, with a duration of 146 s at 60 kV and a pixel size of 80 μm . Further quantitative image analysis was performed with AMIDE software (calculation of percent injected dose per cm^3 (%ID/ cm^3) in region-of-interests (ROIs)), and 3D images were prepared in Osirix software (Pixmeo, Bernex, Switzerland). Radioactive tumor-to-muscle (TMR^{rad}) ratios were determined by dividing the tumor's %ID/ cm^3 by the muscle's %ID/ cm^3 .

Fluorescence imaging was performed using a KIS700 camera (Kaer Labs, Nantes, France), an open surgical system with resolution of 1920×1200 , excitation wavelength of 640 nm and emission light collection above 665 nm (high pass). Background fluorescence (measured without excitation) was subtracted from the images and analysis was performed using ImageJ. For the different ROIs, mean fluorescent intensity (MFI) was calculated. Fluorescent TMR (TMR^{fluo}) ratios were determined by dividing the tumor's MFI values by the muscle's MFI values.

2.6. Statistical Analysis

For the fluorescence *in vitro* functionality assay, results were compared using an ordinary one-way ANOVA, corrected for multiple comparisons. Uptake between HER2-expressing and HER2-negative tumors was compared using an unpaired Student's *t*-test. The correlation between nuclear and fluorescent signals was investigated by linear regression. Statistical analyses were performed using Prism 7 (Graphpad Software, San Diego, CA, USA). All data on the graphs is displayed as the mean \pm SD.

3. Results

3.1. Production, MSAP Conjugation, and Radiolabeling of Nanobodies

Following MSAP conjugation to the 2Rs15d Nanobody, SEC analysis confirmed the purity of MSAP.2Rs15d. The compound eluted as a single peak with a retention time of 6–7 min (as expected for a Nanobody), and absorbing at both 280 and 650 nm. The average DOL was determined to be 1.1 MSAP molecules per Nanobody.

MSAP.2Rs15d could be successfully ^{111}In -labeled, yielding a radiochemical purity of >95% as determined by iTLC. Further quality controls (QC) performed by radio-SEC, confirmed that the radioactive signal matched the retention times of MSAP.2Rs15d (absorbance at 280 and 650 nm) (Figure 2a), and that the tracer remained stable up to at least 24 h incubation in PBS or serum as no degradation of the protein, fluorescent, and/or radioactive signal was seen (Figure 2b,c)

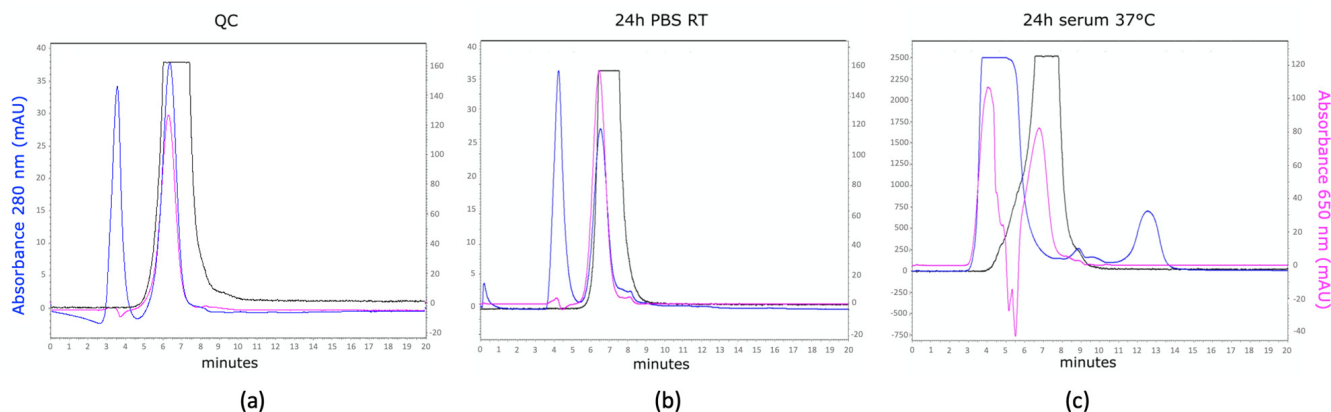


Figure 2. Quality control and stability size-exclusion chromatography (SEC) profiles of [^{111}In]In-MSAP.2Rs15d. (a) SEC profile of MSAP.2Rs15d after radiolabeling with ^{111}In . (b) SEC profile of [^{111}In]In-MSAP.2Rs15d after 24 h incubation in PBS. (c) SEC profile of [^{111}In]In-MSAP.2Rs15d after 24 h incubation in human serum at 37 °C. The blue line denotes absorption at 280 nm, the pink line denotes absorption at 650 nm, and the black line represents the radioactive signal intensity. Both in panel (a,b), [^{111}In]In-MSAP.2Rs15d is dissolved in PBS 0.05% Tween[®] 80; the additional peak seen around 4 min is attributed to the absorbance of Tween 80 at 280 nm. In panel (c), the absorbance of the Nanobody at 280 nm is negligible compared to the intense signal at 280 nm of the serum proteins. Therefore, the stability of the compound is determined based on the presence of the radioactive signal peak and the MSAP absorption peak at 650 nm at 6–7 min, comparable to the profiles in panel (a,b). Furthermore, serum proteins with a retention time of 3–5 min exhibit some autofluorescence at 650 nm, explaining the peak in 650 nm absorbance at 3–5 min.

3.2. In Vitro Functionality

SPR measurements revealed the dissociation constant (K_D) of the MSAP.2Rs15d construct to be $5.0 \pm 0.1 \times 10^{-9}$ M (Figure 3a). Specificity of the construct was further demonstrated by the significantly higher binding to HER2-expressing SKOV3 cells than to non-HER2-expressing CHO cells, or SKOV3 cells incubated with an excess of unlabeled 2Rs15d (Figure 3b). With a K_D of $1.6 \pm 0.2 \times 10^{-9}$ M as determined via a saturation binding assay on SKOV3 cells, it was confirmed that also after ^{111}In -labeling, the affinity of the Nanobody was not negatively affected (Figure 3c). The small difference in K_D measured using SPR and cell-binding studies can be explained by the use of purified recombinant HER2 protein in the case of SPR, and high HER2-overexpressing cells for the radioligand-binding assay. Nevertheless, both values are in the low nanomolar range and comparable to that of the unconjugated 2Rs15d ($3.2 \pm 0.1 \times 10^{-9}$ M) (Figure S1).

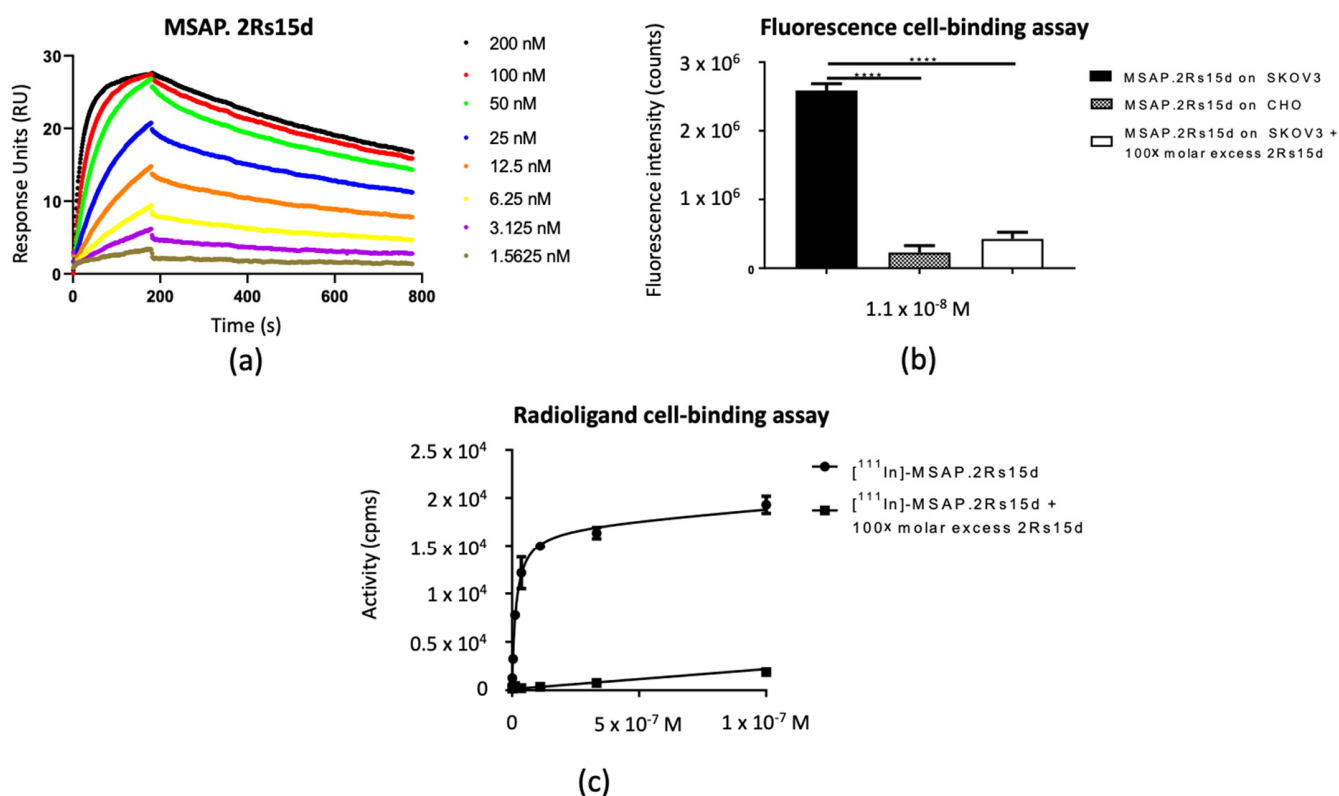


Figure 3. In vitro functionality assays. (a) SPR graphs of MSAP.2Rs15d on the immobilized HER2-Fc protein. (b) Fluorescence cell-binding assay of MSAP.2Rs15d at a fixed concentration of 1.1×10^{-8} M on HER2-expressing SKOV3 cells or HER2-negative CHO cells (**** $p < 0.001$). Data are represented as mean \pm SD ($n = 3$ replicates per condition). (c) Saturation cell-binding assay (radioactive) demonstrating the specificity and high affinity of the $[^{111}\text{In}]\text{In-MSAP.2Rs15d}$ for the HER2-expressing SKOV3 cells. Data are represented as mean \pm SD ($n = 3$ replicates per condition).

3.3. In Vivo Biodistribution and Tumor Targeting Potential Using Bimodal Imaging

3.3.1. Longitudinal Biodistribution in Subcutaneous Xenografts

As shown in Figure 4, SPECT/CT and fluorescence images coincided, and revealed an analogous biodistribution pattern for $[^{111}\text{In}]\text{In-MSAP.2Rs15d}$ at 1 h, 4 h, and 24 h post-injection, with low non-specific uptake in untargeted organs, except for the kidneys due to renal retention of the tracer. SKOV3 tumors could be clearly distinguished as soon as 1 h post-injection, while no uptake in control MDA-MB-435S xenografts was seen (Figure 4a and Figure S2). This was confirmed by quantification of the tumor uptake and tumor-to-muscle ratios (TMRs) based on the SPECT/CT images, yielding significant differences between SKOV3 and MDA-MB-435S at all timepoints (Figure 4b,c). More specifically, in SKOV3 xenografted mice a TMR^{rad} of 19.8 ± 3.8 was achieved within 1 h and preserved over 24 h (21.1 ± 10.5). The absolute specific uptake did gradually decrease over time (Figure 4b) from 2.2 ± 0.5 %ID/cm³ at 1 h to 1.0 ± 0.4 %ID/cm³ at 24 h post-injection. The TMR^{rad} for MDA-MB-435S control tumors was only 1.1 ± 1.0 ($p < 0.05$). On the fluorescent images, tumor uptake in SKOV3 xenografted mice could be clearly visualized with TMR^{fluo} of 4.6 ± 1.5 and 4.5 ± 1.6 at respectively 1 and 4 h. These values were lower than for SPECT/CT imaging in consequence of signal attenuation by tissue and background autofluorescence.

The *in vivo* findings were further confirmed by the *ex vivo* biodistribution analysis after 24 h (Figure 4d, Tables S1 and S2). Indeed, the semiquantitative fluorescent data reflects the trend seen in the quantitative data obtained through gamma counting, with exception of the elevated fluorescent signals in the intestines and stomach (due to mouse chow [37]). The overall tumor uptake after 24 h in SKOV3 xenografts was measured to be 1.5 ± 0.2 %ID/g, which is similar to the *in vivo* measured data. Table S1 further illustrates the high tumor-to-organ ratios.

3.3.2. Image-Guided Resection of Intraperitoneally Disseminated Tumor Lesions

SPECT/CT scans (1 h post-injection) could be used to visualize the largest tumor masses (Figure 5a), however, smaller tumor nodules could not be visualized because of the inherent limited resolution and sensitivity of the imaging technique and shine through of the nearby kidneys. Subsequent opening of the abdominal cavity allowed *in situ* fluorescence-based visualization and fluorescence-guided removal of even submillimeter tumor lesions that were spread at the surface of the animal's peritoneum (38 lesions were removed in total, Figure 5a–c). *Ex vivo* analysis of BLI-confirmed tumor lesions was then used to correlate the uptake of fluorescence and radioactive signals in the resected lesions. The %ID of radioactivity in resected tumor lesions was plotted against their total fluorescence signal (Figure 5d), and after fitting a line with linear regression, an R^2 value of 0.97 was obtained, which indicates the good correlation between both modalities. The biodistribution and tumor-to-organ ratio's obtained through *ex vivo* fluorescence imaging and gamma counting is displayed in Figure S3 and Table S3.

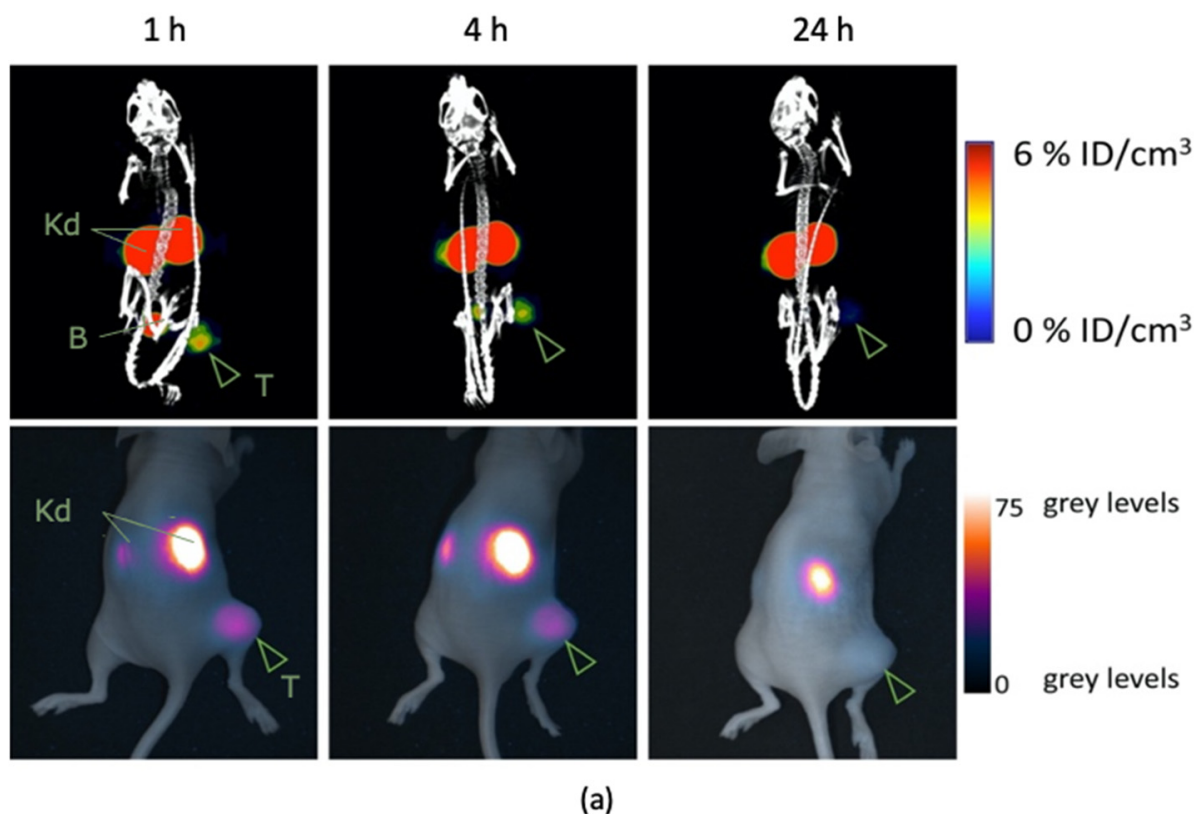


Figure 4. Cont.

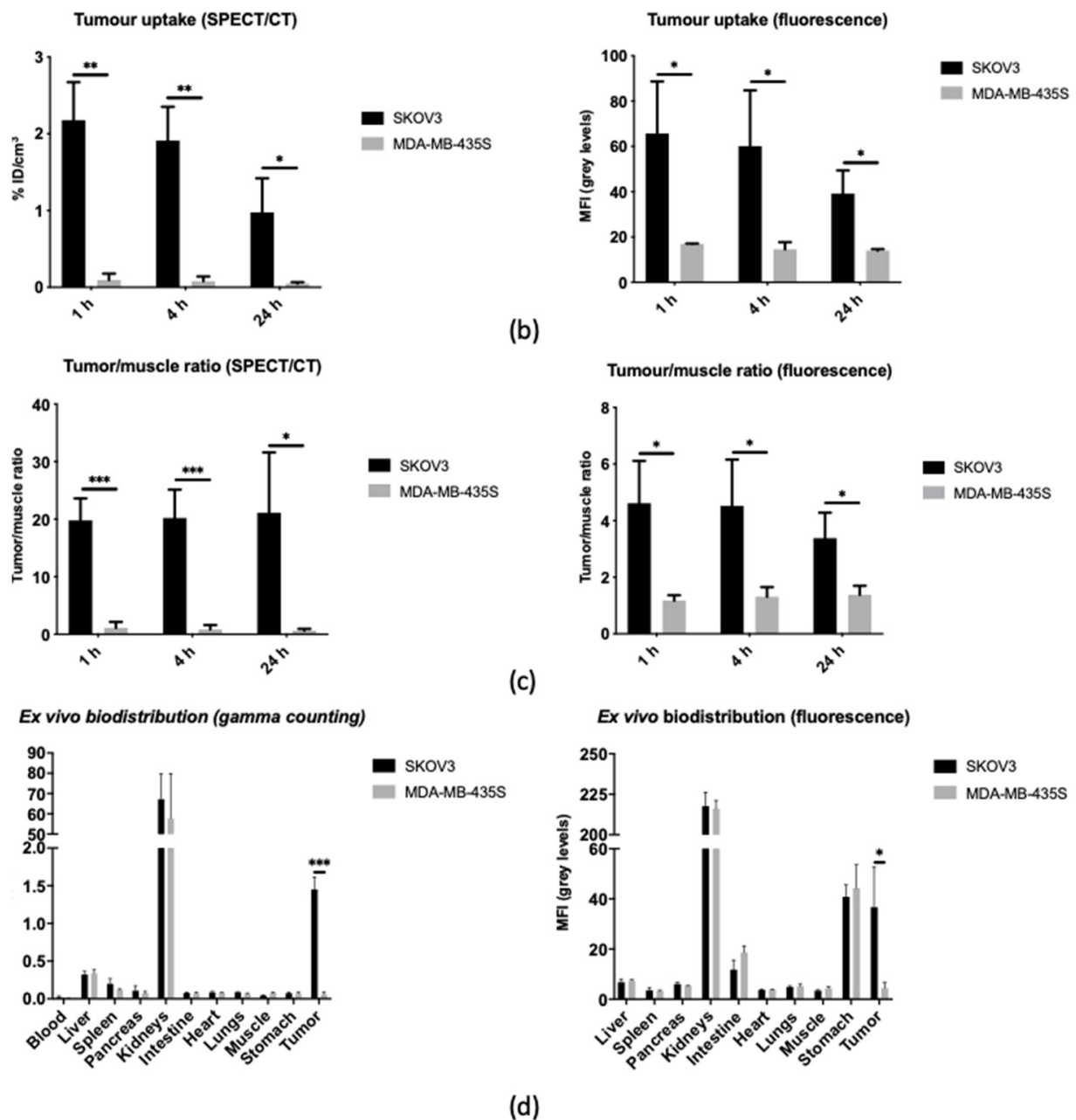


Figure 4. (a) Representative SPECT/CT (top) and fluorescence (bottom) images of a SKOV3 bearing mouse at 1 h, 4 h, and 24 h post-injection of [¹¹¹In]In-MSAP.2Rs15d. Specific uptake can be observed in the tumor (T), with little to no non-specific uptake, except for in the kidneys (Kd) and the bladder (B). This results in the specific and high-contrast imaging of HER2-positive subcutaneous tumors. (b) In vivo quantification of [¹¹¹In]In-MSAP.2Rs15d tumor uptake, based on SPECT/CT (left) or fluorescence (right). SPECT/CT data is represented as % of the initial injected dose per cm³ of tissue (%ID/cm³), whereas the fluorescence data are represented as the mean fluorescence intensity (MFI) of the tumor area (in grey levels) (** *p* < 0.01, * *p* < 0.05). All data is represented as mean ± SD (*n* = 3 mice per group, *N* = 6). (c) In vivo tumor-to-muscle ratios over time measured by SPECT/CT (left) or fluorescence (right) (***) *p* < 0.005, * *p* < 0.05). All data is represented as mean ± SD (*n* = 3 mice per group, *N* = 6). (d) Ex vivo biodistribution of [¹¹¹In]In-MSAP.2Rs15d in SKOV3 and MDA-MB-435S xenograft bearing mice at 24 h post injection. Determined by gamma counting (left) as % injected dose per gram (%ID/g) or by fluorescence measurement (right) as MFI. Both biodistribution profiles match, except for the elevated signal in gastrointestinal organs measured by fluorescence, due to the mouse chow (***) *p* < 0.005, * *p* < 0.05). All data is represented as mean ± SD (*n* = 3 mice per group, *N* = 6).

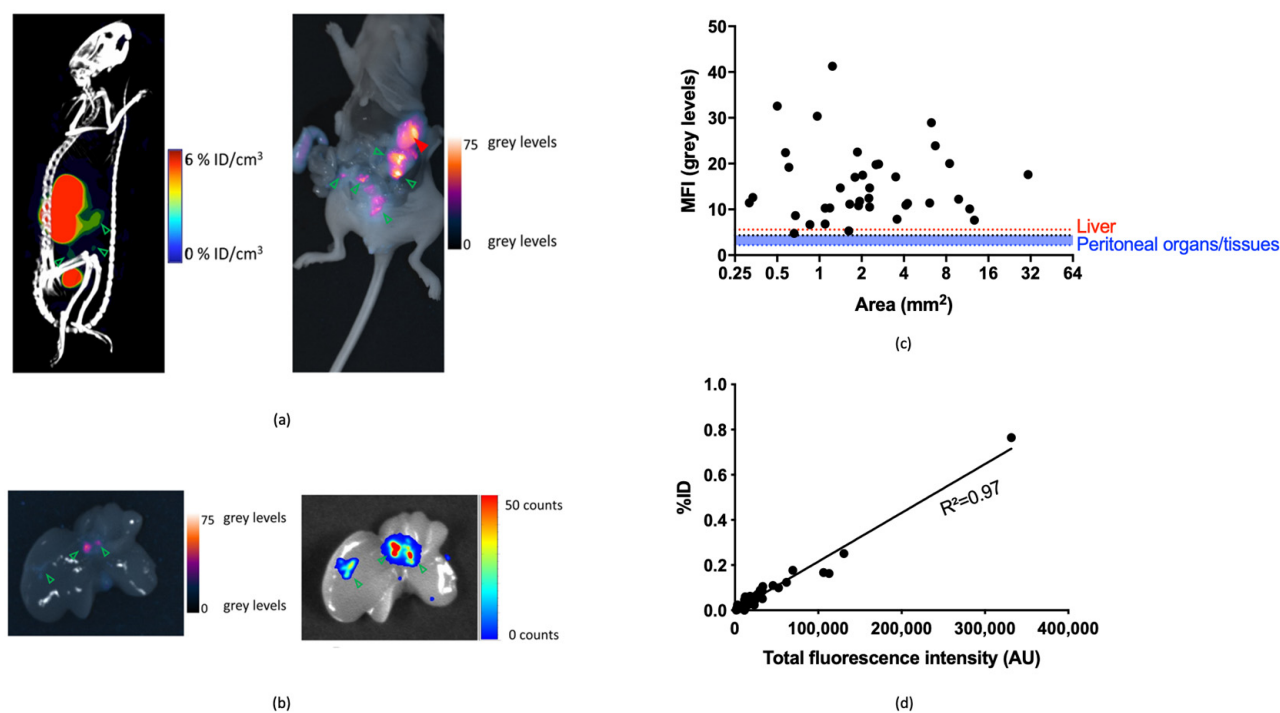


Figure 5. (a) Representative SPECT/CT (left) and fluorescence (right) scan of a mouse bearing intraperitoneally disseminated SKOV3.IP1 tumor lesions at 1 h post-injection of $[^{111}\text{In}]\text{In-MSAP.2Rs15d}$. Tumor tissue is denoted by green arrows, the stomach is indicated by a red arrow. (b) Ex vivo liver with tumor nodules visualized by fluorescence imaging (left) and confirmed by BLI (right). Some non-specific fluorescence is seen due to the gallbladder. Tumor tissue is denoted by green arrows. (c) Mean fluorescence intensity (MFI) of individual SKOV3.IP1 tumor lesions as a function of their size. MFI is displayed relative to the average MFI of relevant peritoneal organs and tissues (spleen, pancreas, intestine, and muscle; blue line) and of the liver (red line) ($n = 3$ mice per group, $N = 3$). (d) Correlation of radioactive and fluorescent signals. The total %ID of radioactivity is plotted against the fluorescence intensity over the whole tumor area. A linear relationship is seen between both modalities, indicating a good correspondence of the signals ($n = 3$ mice per group, $N = 3$).

4. Discussion

Fluorescence surgical guidance has potential to improve the detection and removal of cancerous tissue, however, the technique is held back by unfavorable interaction of light and tissue (attenuation and scattering). Therefore, the use of bimodal labels such as the MSAP analogues, combining fluorescence and nuclear imaging may help overcome this limitation. Such a combination has been shown to allow pre/intraoperative detection of disease in a depth-independent manner and thus facilitates surgical navigation [3]. We here demonstrated that this concept can also be used to advance the use of Nanobodies in molecular imaging towards such bimodal applications.

We showed that an MSAP analogue carrying both a Cy5 fluorescent dye and a DTPA chelator for ^{111}In -labeling could be readily conjugated to a HER2-specific Nanobody without impacting its affinity or its pharmacokinetics. Administration of a single dose of the tracer resulted in high-contrast and specific visualization of HER2-expressing tumors via both SPECT/CT and fluorescence imaging (1–24 h p.i.), and with the exception of the kidneys, little to no non-specific uptake in HER2-negative tumors or non-targeted tissues. This corroborates with previous biodistribution profiles obtained after labeling of the same Nanobody with various PET, SPECT, or therapeutic radioisotopes [32,33,38–41], and is in stark contrast with the drastic effect random labeling with the heptamethine fluorophore IRDye800CW has on the biodistribution of Nanobodies (high non-specific uptake and hepatic clearance [29]). The high fluorescent signal in the kidneys as observed in mice will most likely pose no problems in patients due to the attenuation of the signal by perinephric fat. However, the radioactive signal originating from the kidneys may create

a significant background signal and affect adjacent tumor lesion detection. The use of Gelofusin or positively charged amino acids have been shown to reduce kidney retention in previous studies and could possibly be applied to counteract this limitation [42]. In the future, site-specific conjugation methods using cysteine-maleimide chemistry [41] or using the enzyme Sortase [40] could be considered to further standardize the tracer's composition if needed. Additional improvements can be found in minimizing the bimodal labels and using chelates that allow radiolabeling with ^{99m}Tc , a radioisotope with more translational potential [43].

The proof-of-concept study in a murine model of intraperitoneally disseminated cancer showed that addition of a nuclear modality to the fluorescent component can further extend the potential of Nanobody-based imaging. Besides improvement of the characterization process and enabling a more exact determination of the tracer's biodistribution, [^{111}In]In-MSAP.2Rs15d could be used for both preoperative planning, and for precise and sensitive guidance during the actual surgical intervention. Indeed, preoperative nuclear medicine imaging can provide useful information on the anatomical localization of the tumor lesions and lymph node metastases [44]. Radioguided surgery solutions in the form of intraoperative gamma tracing can help to further guide the surgeon towards cancerous lesions, a concept that is currently being explored for prostate cancer [45]. A limitation of the study is certainly the choice of HER2 as biomarker, given its overexpression in a restricted number of cancer types and its intratumoral heterogeneity [46].

5. Conclusions

In this study we described the preparation of a bimodal nuclear/fluorescent Nanobody-tracer through the convenient conjugation of a single-molecule MSAP-reagent carrying both a fluorophore and chelator for radioactive labeling. The Nanobody-tracer possessed an adequate biodistribution profile enabling fast and high-contrast nuclear and fluorescent imaging with low background. Such a tracer holds promise for clinical application in the context of image-guided surgery as was demonstrated by a proof-of-concept study in which intraperitoneally tumor lesions could be localized preoperatively using SPECT/CT, and then precisely excised via intraoperative fluorescence imaging.

Supplementary Materials: The following are available online at <https://www.mdpi.com/2218-273X/11/3/360/s1>, Figure S1: SPR graphs of reference unconjugated 2Rs15d on immobilized HER2-Fc protein, Figure S2: SPECT/CT (a) and fluorescence (b) images of mice bearing MDA-MB-435S xenografts, Table S1: Tumor-to-organ ratios calculated from ex vivo biodistribution at 24 h post-injection of [^{111}In]MSAP.2Rs15d in mice bearing subcutaneous SKOV3 xenografts, Table S2: Tumor-to-organ ratios calculated from ex vivo biodistribution at 24 h post-injection of [^{111}In]MSAP.2Rs15d in mice bearing subcutaneous MDA-MB-435S xenografts, Figure S3: Ex vivo biodistribution of mice bearing SKOV3.IP1 intraperitoneally disseminated tumor lesions as determined by SPECT/CT and fluorescence imaging, Table S3: Tumor-to-organ ratios calculated from ex vivo biodistribution at 1 h post-injection of [^{111}In]MSAP.2Rs15d in mice bearing intraperitoneally disseminated SKOV3.IP1 tumors, Figure S4: Ex vivo imaging of resected pancreas from SKOV3.IP1 intraperitoneally disseminated tumor bearing mouse.

Author Contributions: Conceptualization, P.D. and S.H.; Data curation, P.D.; Funding acquisition, P.D., N.B.D. and S.H.; Investigation, C.M.H., B.D.S., L.M., J.B. and J.P.; Methodology, P.D.; Supervision, N.D. and F.W.B.v.L.; Writing—original draft, P.D.; Writing—review and editing, P.D., N.B.D., D.v.W., N.D., F.W.B.v.L. and S.H. All authors have read and agreed to the published version of the manuscript.

Funding: This research was funded by a grant from 'Stichting tegen Kanker' (FAF-C/2016/813). P. Debie has received personal funding from the Oncology Research Centre (ORC) of the Universitair Ziekenhuis Brussel (UZ Brussel). N. Declerck has received a personal grant from the 'Fonds Wetenschappelijk Onderzoek' of Flanders (FWOSB74). J. Bridoux has received funding from the Scientific Fund W. Gepts (UZ Brussel).

Institutional Review Board Statement: All animal study protocols were approved by the Ethical Committee for Animal Experiments of the Vrije Universiteit Brussel (project nr. 15-272-5).

Informed Consent Statement: Not applicable.

Data Availability Statement: Data sharing is not applicable for this article. All data is contained within the article or supplementary material. The data presented in this study are available in ‘The Design and Preclinical Evaluation of a Single-Label Bi-modal Nanobody Tracer for Image-Guided Surgery—Supplementary data’.

Acknowledgments: We thank Cindy Peleman, Jan De Jonge and Kevin De Jonghe for their assistance with the practical work. We thank Fleur De Boe for her help with the animal care.

Conflicts of Interest: N. Devoogdt hold ownership interest in Abscint NV/SA. G. N. Devoogdt is consultant for and hold ownership interest in Precirix NV/SA.

References

1. Hernot, S.; Van Manen, L.; Debie, P.; Mieog, J.S.D.; Vahrmeijer, A.L. Latest developments in molecular tracers for fluorescence image-guided cancer surgery. *Lancet Oncol.* **2019**, *20*, e354–e367. [[CrossRef](#)]
2. Berg, N.S.V.D.; Brouwer, O.R.; Schaafsma, B.E.; Mathéron, H.M.; Klop, W.M.C.; Balm, A.J.M.; Van Tinteren, H.; Nieweg, O.E.; Van Leeuwen, F.W.B.; Olmos, R.A.V. Multimodal Surgical Guidance during Sentinel Node Biopsy for Melanoma: Combined Gamma Tracing and Fluorescence Imaging of the Sentinel Node through Use of the Hybrid Tracer Indocyanine Green–99mTc-Nanocolloid. *Radiology* **2015**, *275*, 521–529. [[CrossRef](#)]
3. Van Leeuwen, F.W.; Schottelius, M.; Brouwer, O.R.; Vidal-Sicart, S.; Achilefu, S.; Klode, J.; Wester, H.-J.; Buckle, T. Trending: Radioactive and Fluorescent Bimodal/Hybrid Tracers as Multiplexing Solutions for Surgical Guidance. *J. Nucl. Med.* **2019**, *61*, 13–19. [[CrossRef](#)] [[PubMed](#)]
4. Dell’Oglio, P.; de Vries, H.M.; Mazzone, E.; KleinJan, G.H.; Donswijk, M.L.; van der Poel, H.G.; Horenblas, S.; van Leeuwen, F.W.; Brouwer, O.R. Hybrid Indocyanine Green–99mTc-nanocolloid for Single-photon Emission Computed Tomography and Combined Radio- and Fluorescence-guided Sentinel Node Biopsy in Penile Cancer: Results of 740 Inguinal Basins Assessed at a Single Institution. *Eur. Urol.* **2020**, *78*, 865–872. [[CrossRef](#)] [[PubMed](#)]
5. De Gooyer, J.M.; Elekonawo, F.M.; Bos, D.L.; Van Der Post, R.S.; Pèlerin, A.; Framery, B.; Cailler, F.; Vahrmeijer, A.L.; De Wilt, J.H.; Rijpkema, M. Multimodal CEA-Targeted Image-Guided Colorectal Cancer Surgery using 111In-Labeled SGM-101. *Clin. Cancer Res.* **2020**, *26*, 5934–5942. [[CrossRef](#)] [[PubMed](#)]
6. Hekman, M.C.; Rijpkema, M.; Muselaers, C.H.; Oosterwijk, E.; De Kaa, C.A.H.-V.; Boerman, O.C.; Oyen, W.J.; Langenhuijsen, J.F.; Mulders, P.F. Tumor-targeted Dual-modality Imaging to Improve Intraoperative Visualization of Clear Cell Renal Cell Carcinoma: A First in Man Study. *Theranostics* **2018**, *8*, 2161–2170. [[CrossRef](#)]
7. Van Leeuwen, F.W.; Valdés-Olmos, R.; Buckle, T.; Vidal-Sicart, S. Hybrid surgical guidance based on the integration of radionuclear and optical technologies. *Br. J. Radiol.* **2016**, *89*, 20150797. [[CrossRef](#)] [[PubMed](#)]
8. Folli, S.; Wagnieres, G.; Pelegrin, A.; Calmes, J.M.; Braichotte, D.; Buchegger, F.; Chalandon, Y.; Hardman, N.; Heusser, C.; Givel, J.C. Immunophotodiagnosis of colon carcinomas in patients injected with fluoresceinated chimeric antibodies against carcinoembryonic antigen. *Proc. Natl. Acad. Sci. USA* **1992**, *89*, 7973–7977. [[CrossRef](#)] [[PubMed](#)]
9. Cohen, R.; Stammes, M.A.; De Roos, I.H.; Walsum, M.S.-V.; Visser, G.W.; Van Dongen, G.A. Inert coupling of IRDye800CW to monoclonal antibodies for clinical optical imaging of tumor targets. *EJNMMI Res.* **2011**, *1*, 31. [[CrossRef](#)] [[PubMed](#)]
10. Hekman, M.C.; Rijpkema, M.; Bos, D.L.; Oosterwijk, E.; Goldenberg, D.M.; Mulders, P.F.; Boerman, O.C. Detection of Micrometastases Using SPECT/Fluorescence Dual-Modality Imaging in a CEA-Expressing Tumor Model. *J. Nucl. Med.* **2017**, *58*, 706–710. [[CrossRef](#)]
11. Tsai, W.K.; Zettlitz, K.A.; Tavaré, R.; Kobayashi, N.; Reiter, R.E.; Wu, A.M. Dual-Modality ImmunoPET/Fluorescence Imaging of Prostate Cancer with an Anti-PSCA Cys-Minibody. *Theranostics* **2018**, *8*, 5903–5914. [[CrossRef](#)]
12. Bunschoten, A.; Buckle, T.; Visser, N.L.; Kuil, J.; Yuan, H.; Josephson, L.; Vahrmeijer, A.L.; van Leeuwen, F.W. Multimodal interventional molecular imaging of tumor margins and distant metastases by targeting alphavbeta3 integrin. *Chembiochem* **2012**, *13*, 1039–1045. [[CrossRef](#)]
13. Garanger, E.; Aikawa, E.; Reynolds, F.; Weissleder, R.; Josephson, L. Simplified syntheses of complex multifunctional nanomaterials. *Chem. Commun.* **2008**, *39*, 4792–4794. [[CrossRef](#)] [[PubMed](#)]
14. Kuil, J.; Buckle, T.; Yuan, H.; Berg, N.S.V.D.; Oishi, S.; Fujii, N.; Josephson, L.; Van Leeuwen, F.W.B. Synthesis and Evaluation of a Bimodal CXCR4 Antagonistic Peptide. *Bioconjugate Chem.* **2011**, *22*, 859–864. [[CrossRef](#)] [[PubMed](#)]
15. Buckle, T.; Kuil, J.; Berg, N.S.V.D.; Bunschoten, A.; Lamb, H.J.; Yuan, H.; Josephson, L.; Jonkers, J.; Borowsky, A.D.; Van Leeuwen, F.W.B. Use of a Single Hybrid Imaging Agent for Integration of Target Validation with In Vivo and Ex Vivo Imaging of Mouse Tumor Lesions Resembling Human DCIS. *PLoS ONE* **2013**, *8*, e48324. [[CrossRef](#)] [[PubMed](#)]
16. Guo, Y.; Yuan, H.; Rice, W.L.; Kumar, A.T.N.; Goergen, C.J.; Jokivarsi, K.; Josephson, L. The PEG-Fluorochrome Shielding Approach for Targeted Probe Design. *J. Am. Chem. Soc.* **2012**, *134*, 19338–19341. [[CrossRef](#)] [[PubMed](#)]
17. Bunschoten, A.; Van Willigen, D.M.; Buckle, T.; Berg, N.S.V.D.; Welling, M.M.; Spa, S.J.; Wester, H.-J.; Van Leeuwen, F.W.B. Tailoring Fluorescent Dyes To Optimize a Hybrid RGD-Tracer. *Bioconjugate Chem.* **2016**, *27*, 1253–1258. [[CrossRef](#)] [[PubMed](#)]

18. Buckle, T.; van Willigen, D.M.; Spa, S.J.; Hensbergen, A.W.; van der Wal, S.; de Korne, C.M.; Welling, M.M.; van der Poel, H.G.; Hardwick, J.C.H.; van Leeuwen, F.W.B. Tracers for Fluorescence-Guided Surgery: How Elongation of the Polymethine Chain in Cyanine Dyes Alters the Pharmacokinetics of a Dual-Modality c[RGDyK] Tracer. *J. Nucl. Med.* **2018**, *59*, 986–992. [[CrossRef](#)]
19. Boonstra, M.C.; van Driel, P.B.; van Willigen, D.M.; Stammes, M.A.; Prevo, H.A.; Tummers, Q.R.; Mazar, A.P.; Beekman, F.J.; Kuppen, P.J.; van de Velde, C.J.; et al. uPAR-targeted multimodal tracer for pre- and intraoperative imaging in cancer surgery. *Oncotarget* **2015**, *6*, 14260–14273. [[CrossRef](#)] [[PubMed](#)]
20. Boonstra, M.C.; Van Driel, P.B.; Keereweer, S.; Prevo, H.A.; Stammes, M.A.; Baart, V.M.; Lowik, C.W.; Mazar, A.P.; van de Velde, C.J.; Vahrmeijer, A.L.; et al. Preclinical uPAR-targeted multimodal imaging of locoregional oral cancer. *Oral Oncol.* **2017**, *66*, 1–8. [[CrossRef](#)] [[PubMed](#)]
21. Wu, A.M.; Olafsen, T. Antibodies for Molecular Imaging of Cancer. *Cancer J.* **2008**, *14*, 191–197. [[CrossRef](#)] [[PubMed](#)]
22. Hamers-Casterman, C.; Atarhouch, T.; Muyldermans, S.; Robinson, G.; Hammers, C.; Songa, E.B.; Bendahman, N.; Hammers, R. Naturally occurring antibodies devoid of light chains. *Nature* **1993**, *363*, 446–448. [[CrossRef](#)] [[PubMed](#)]
23. Ingram, J.R.; Schmidt, F.I.; Ploegh, H.L. Exploiting Nanobodies' Singular Traits. *Annu. Rev. Immunol.* **2018**, *36*, 695–715. [[CrossRef](#)] [[PubMed](#)]
24. Debie, P.; Devoogdt, N.; Hernot, S. Targeted Nanobody-Based Molecular Tracers for Nuclear Imaging and Image-Guided Surgery. *Antibodies* **2019**, *8*, 12. [[CrossRef](#)]
25. Chakravarty, R.; Goel, S.; Cai, W. Nanobody: The “Magic Bullet” for Molecular Imaging? *Theranostics* **2014**, *4*, 386–398. [[CrossRef](#)] [[PubMed](#)]
26. Krasniqi, A.; D’Huyvetter, M.; Devoogdt, N.; Frejd, F.Y.; Sorensen, J.; Orlova, A.; Keyaerts, M.; Tolmachev, V. Same-Day Imaging Using Small Proteins: Clinical Experience and Translational Prospects in Oncology. *J. Nucl. Med.* **2018**, *59*, 885–891. [[CrossRef](#)]
27. Oliveira, S.; Van Dongen, G.A.; Walsum, M.S.-V.; Roovers, R.C.; Stam, J.C.; Mali, W.; Van Diest, P.J.; Henegouwen, P.M.V.B.E. Rapid Visualization of Human Tumor Xenografts through Optical Imaging with a Near-Infrared Fluorescent Anti-Epidermal Growth Factor Receptor Nanobody. *Mol. Imaging* **2012**, *11*, 33–46. [[CrossRef](#)] [[PubMed](#)]
28. Debie, P.; Lafont, C.; Defrise, M.; Hansen, I.; van Willigen, D.M.; van Leeuwen, F.W.; Gijsbers, R.; D’Huyvetter, M.; Devoogdt, N.; Lahoutte, T.; et al. Size and affinity kinetics of nanobodies influence targeting and penetration of solid tumours. *J. Control. Release* **2020**, *317*, 34–42. [[CrossRef](#)] [[PubMed](#)]
29. Debie, P.; Van Quathem, J.; Hansen, I.; Bala, G.; Massa, S.; Devoogdt, N.; Xavier, C.; Hernot, S. Effect of Dye and Conjugation Chemistry on the Biodistribution Profile of Near-Infrared-Labeled Nanobodies as Tracers for Image-Guided Surgery. *Mol. Pharm.* **2017**, *14*, 1145–1153. [[CrossRef](#)]
30. Debie, P.; Vanhoeij, M.; Poortmans, N.; Puttemans, J.; Gillis, K.; Devoogdt, N.; Lahoutte, T.; Hernot, S. Improved Debulking of Peritoneal Tumor Implants by Near-Infrared Fluorescent Nanobody Image Guidance in an Experimental Mouse Model. *Mol. Imaging Biol.* **2017**, *20*, 361–367. [[CrossRef](#)] [[PubMed](#)]
31. Keyaerts, M.; Xavier, C.; Heemskerk, J.; Devoogdt, N.; Everaert, H.; Ackaert, C.; Vanhoeij, M.; Duhoux, F.P.; Gevaert, T.; Simon, P.; et al. Phase I Study of ⁶⁸Ga-HER2-Nanobody for PET/CT Assessment of HER2 Expression in Breast Carcinoma. *J. Nucl. Med.* **2015**, *57*, 27–33. [[CrossRef](#)]
32. Vaneycken, I.; Devoogdt, N.; Van Gassen, N.; Vincke, C.; Xavier, C.; Wernery, U.; Muyldermans, S.; Lahoutte, T.; Cavelliers, V. Preclinical screening of anti-HER2 nanobodies for molecular imaging of breast cancer. *FASEB J.* **2011**, *25*, 2433–2446. [[CrossRef](#)] [[PubMed](#)]
33. Xavier, C.; Vaneycken, I.; D’Huyvetter, M.; Heemskerk, J.; Keyaerts, M.; Vincke, C.; Devoogdt, N.; Muyldermans, S.; Lahoutte, T.; Cavelliers, V. Synthesis, Preclinical Validation, Dosimetry, and Toxicity of ⁶⁸Ga-NOTA-Anti-HER2 Nanobodies for iPET Imaging of HER2 Receptor Expression in Cancer. *J. Nucl. Med.* **2013**, *54*, 776–784. [[CrossRef](#)] [[PubMed](#)]
34. Spa, S.; Hensbergen, A.; Van Der Wal, S.; Kuil, J.; Van Leeuwen, F. The influence of systematic structure alterations on the photophysical properties and conjugation characteristics of asymmetric cyanine 5 dyes. *Dye. Pigment.* **2018**, *152*, 19–28. [[CrossRef](#)]
35. Bala, G.; Crauwels, M.; Blykers, A.; Remory, I.; Marschall, A.L.; Dübel, S.; Dumas, L.; Broisat, A.; Martin, C.; Ballet, S.; et al. Radiometal-labeled anti-VCAM-1 nanobodies as molecular tracers for atherosclerosis—impact of radiochemistry on pharmacokinetics. *Biol. Chem.* **2019**, *400*, 323–332. [[CrossRef](#)] [[PubMed](#)]
36. De Vlieghe, E.; Carlier, C.; Ceelen, W.; Bracke, M.; De Wever, O. Data on in vivo selection of SK-OV-3 Luc ovarian cancer cells and intraperitoneal tumor formation with low inoculation numbers. *Data Brief* **2016**, *6*, 542–549. [[CrossRef](#)]
37. Bhaumik, S.; DePuy, J.; Klimash, J. Strategies to minimize background autofluorescence in live mice during noninvasive fluorescence optical imaging. *Lab Anim.* **2007**, *36*, 40–43. [[CrossRef](#)] [[PubMed](#)]
38. Xavier, C.; Blykers, A.; Vaneycken, I.; D’Huyvetter, M.; Heemskerk, J.; Lahoutte, T.; Devoogdt, N.; Cavelliers, V. ¹⁸F-nanobody for PET imaging of HER2 overexpressing tumors. *Nucl. Med. Biol.* **2016**, *43*, 247–252. [[CrossRef](#)] [[PubMed](#)]
39. D’Huyvetter, M.; De Vos, J.; Xavier, C.; Pruszynski, M.; Sterckx, Y.G.J.; Massa, S.; Raes, G.; Cavelliers, V.; Zalutsky, M.R.; Lahoutte, T.; et al. ¹³¹I-labeled Anti-HER2 Camelid sdAb as a Theranostic Tool in Cancer Treatment. *Clin. Cancer Res.* **2017**, *23*, 6616–6628. [[CrossRef](#)]
40. Massa, S.; Vikani, N.; Betti, C.; Ballet, S.; Vanderhaegen, S.; Steyaert, J.; Descamps, B.; Vanhove, C.; Bunschoten, A.; Van Leeuwen, F.W.B.; et al. Sortase A-mediated site-specific labeling of camelid single-domain antibody-fragments: A versatile strategy for multiple molecular imaging modalities. *Contrast Media Mol. Imaging* **2016**, *11*, 328–339. [[CrossRef](#)]

41. Massa, S.; Xavier, C.; De Vos, J.; Caveliers, V.; Lahoutte, T.; Muyldermans, S.; Devoogdt, N. Site-Specific Labeling of Cysteine-Tagged Camelid Single-Domain Antibody-Fragments for Use in Molecular Imaging. *Bioconjugate Chem.* **2014**, *25*, 979–988. [[CrossRef](#)] [[PubMed](#)]
42. Gaikam, L.O.T.; Caveliers, V.; Devoogdt, N.; Vanhove, C.; Xavier, C.; Boerman, O.; Muyldermans, S.; Bossuyt, A.; Lahoutte, T. Localization, mechanism and reduction of renal retention of technetium-99m labeled epidermal growth factor receptor-specific nanobody in mice. *Contrast Media Mol. Imaging* **2010**, *6*, 85–92. [[CrossRef](#)] [[PubMed](#)]
43. Hensbergen, A.W.; Buckle, T.; van Willigen, D.M.; Schottelius, M.; Welling, M.M.; van der Wijk, F.A.; Maurer, T.; van der Poel, H.G.; van der Pluijm, G.; van Weerden, W.M.; et al. Hybrid Tracers Based on Cyanine Backbones Targeting Prostate-Specific Membrane Antigen: Tuning Pharmacokinetic Properties and Exploring Dye-Protein Interaction. *J. Nucl. Med.* **2020**, *61*, 234–241. [[CrossRef](#)] [[PubMed](#)]
44. Stoffels, I.; Boy, C.; Pöppel, T.; Kuhn, J.; Klötgen, K.; Dissemond, J.; Schadendorf, D.; Klode, J. Association Between Sentinel Lymph Node Excision With or Without Preoperative SPECT/CT and Metastatic Node Detection and Disease-Free Survival in Melanoma. *JAMA* **2012**, *308*, 1007–1014. [[CrossRef](#)] [[PubMed](#)]
45. Maurer, T.; Robu, S.; Schottelius, M.; Schwamborn, K.; Rauscher, I.; Berg, N.S.V.D.; van Leeuwen, F.W.; Haller, B.; Horn, T.; Heck, M.M.; et al. ^{99m}Techetium-based Prostate-specific Membrane Antigen–radioguided Surgery in Recurrent Prostate Cancer. *Eur. Urol.* **2019**, *75*, 659–666. [[CrossRef](#)] [[PubMed](#)]
46. English, D.P.; Roque, D.M.; Santin, A.D. HER2 Expression Beyond Breast Cancer: Therapeutic Implications for Gynecologic Malignancies. *Mol. Diagn. Ther.* **2013**, *17*, 85–99. [[CrossRef](#)] [[PubMed](#)]